PCCP

ROYAL SOCIETY OF CHEMISTRY

PAPER

View Article Online
View Journal | View Issue

Cite this: *Phys. Chem. Chem. Phys.*, 2022, **24**, 11249

Theoretical predictions of phase stability for orthorhombic and hexagonal ternary MAB phases†

Adam Carlsson, Johanna Rosen and Martin Dahlqvist *

Received 16th December 2021,
Accepted 11th April 2022

DOI: 10.1039/d1cp05750b

rsc.li/pccp

In the quest for finding novel thermodynamically stable, layered, MAB phases promising for synthesis, we herein explore the phase stability of ternary MAB phases by considering both orthorhombic and hexagonal crystal symmetries for various compositions (MAB, M_2AB_2, M_3AB_4, M_4AB_4, and M_4AB_6 where M = Sc, Y, Ti, Zr, Hf, V, Nb, Ta, Cr, Mo, W, Mn, Fe, and Co, A = Al, Ga, and In, and B is boron). The thermodynamic stability of seven previously synthesized MAB phases is confirmed, three additional phases are predicted to be stable, and 23 phases are found to be close to stable. Furthermore, the crystal symmetry preference for forming orthorhombic or hexagonal crystal structures is investigated where the considered Al-based MAB phases tend to favour orthorhombic structures whereas Ga- and In-based phases in general prefer hexagonal structures. The theoretically predicted stable MAB phases along with the structural preference is intended to both guide experimental efforts and to give an insight into the stability for different crystal symmetries of MAB phases.

Introduction

MAB phases are members of the nanolaminated crystal compound family. In addition to being layered borides, which, as of late, have attracted renewed interest due to their important properties, *i.e.*, exfoliation potential towards two-dimensional (2D) materials,[1] high melting points and high hardness.[2] The mechanical properties of borides in general make them prominent candidates in application areas such as cutting tools[3] and other wear-resistant coatings,[4,5] which motivates the investigation of new stable MAB phases. The possibility of exfoliating MAB phases into their two-dimensional counterparts has been investigated theoretically.[6–8] Experimentally, partial etching has been demonstrated,[9–11] and only recently, Jie *et al.* successfully demonstrated the synthesis of a 2D transition metal boride $Mo_{3/4}B_{2-x}T_z$ by selectively etching Y and Al from the in-plane ordered $(Mo_{2/3}Y_{1/3})_2AlB_2$ and Sc and Al from $(Mo_{2/3}Sc_{1/3})_2AlB_2$.[1] The discovery of $Mo_{3/4}B_{2-x}T_z$ boridene suggests a wealth of future 2D materials.

Similar to MAB phases are the well-known nanolaminated MAX phases, where X, in contrast to B, refers to carbon and/or nitrogen.[12] Like MAB phases, MAX phases are composed of alternating M–X layers interleaved by A-layers. These materials can be exfoliated into 2D MXenes with potential for use in energy storage and electromagnetic shielding.[13,14]

Both MAX and MAB phases were discovered in the 60s.[15,16] MAX phases have since then been demonstrated to encompass a large variety of chemical compositions,[17] in contrast to MAB phases which include fewer elemental combinations but with a larger structural variation. One of the general formulae of MAB phases is $M_{n+1}AB_{2n}$ which covers most compositions where M corresponds to a transition metal, A represents a Group 13 element, B is boron and n = 1, 2, and 3. Generally, MAB phases have alternating stacks of M–B layers interleaved by A-layers. However, additional multilayered compositions which do not fit this general formulation are MAB and M_4AB_4 comprised of double layers of A- and M-elements, respectively.

The stoichiometries considered in this work are based on the synthesized MoAlB and WAlB with orthorhombic space group symmetry (*Cmcm*); Cr_2AlB_2, Mn_2AlB_2 and Fe_2AlB_2 (*Cmmm*), Cr_3AlB_4 (*Pmmm*) and Cr_4AlB_6 (*Cmmm*), respectively.[18] Additionally, in 2019, the field of ternary MAB phases expanded with the discovery of Cr_4AlB_4 with orthorhombic space group symmetry (*Immm*)[19] and Ti_2InB_2 with hexagonal symmetry ($P\bar{6}m2$).[10] The discovery of a hexagonal MAB phase demonstrated that hypothetical MAB phases may potentially crystallize in either orthorhombic or hexagonal symmetry depending on its composition. Our intention is to demonstrate that theory can be used to elucidate compositions favouring a certain symmetry and more importantly if it is stable and thus a suitable candidate for future synthesis.

Materials Design, Department of Physics, Chemistry and Biology (IFM), Linköping University, SE-581 83, Linköping, Sweden. E-mail: adam.carlsson@liu.se, martin.dahlqvist@liu.se

† Electronic supplementary information (ESI) available. See DOI: https://doi.org/10.1039/d1cp05750b

In this work we have performed a screening study on stability for various MAB phase compositions (MAB, M_2AB_2, M_3AB_4, M_4AB_4, and M_4AB_6) by considering both known and manually designed orthorhombic and hexagonal crystal structure symmetries. This is in order to reveal any possible expansion of the family of ternary MAB phases. The screening study includes metals M = Sc, Y, Ti, Zr, Hf, V, Nb, Ta, Cr, Mo, W, Mn, Fe, and Co and the A-elements A = Al, Ga, and In. We verify the stability for seven experimentally known MAB phases and predict the hypothetical Hf_2InB_2, Zr_2InB_2 and Mo_4AlB_4 to be stable. 23 additional phases are found to be close to stable.

Furthermore, additional pathways have previously been suggested as a substitute to thermodynamical stability calculations for identifying candidate MAB phases. Zhang *et al.* used descriptors like atomic size and electron concentration in an attempt to identify stable MAX phases.[20] Shen *et al.* used a similar approach when investigating magnetic MAB phases.[21] Additionally, similar methods have been used in an attempt to effortlessly identify the material properties.[22–24] We challenge the use of such an approach since we find no distinct relation between the considered descriptors and their calculated phase stability.

Theoretical details

Density functional theory calculations

All first principles calculations were performed based on density functional theory (DFT) along with the projector augmented wave potential (PAW) method[25,26] with a plane-wave cutoff energy set to 400 eV. The Vienna *Ab Initio* Simulation Package (VASP) version 5.4.1 was utilized[27,28] with the electronic exchange–correlation interactions described by the generalized gradient approximation (GGA) as parameterized by Perdew–Burke–Ernzerhof (PBE).[29] The use of different exchange correlation functionals has been demonstrated to have a minor influence on the formation enthalpy.[30] Spin-polarization was considered for phases including Cr, Mn, Fe and Co elements in which all non-equivalent collinear magnetic spin configurations within the unit cell were considered for the competing phases. Magnetic spin configurations modelled for the MAB phase structures considered in this work are shown in Fig. S1–S4 (ESI†). The lowest energy spin configuration for each magnetic MAB phase is given in Table S1 (ESI†) where a majority of the phases (43 out of 60) are found to have an AFM configuration as the lowest energy. The identified spin configuration with the lowest energy represents the energy of the considered phase. It should be noted that a potential spin configuration of lower energy for the MAB phase will only stabilize the phase further, *i.e.*, the stable MAB phase predicted here will remain stable even if the detailed magnetic ground state has not been identified. The Brillouin zone was sampled using the Monkhorst–Pack scheme with a *k*-point density of 0.1 $Å^{-1}$.[31] The chosen *k*-point density and cutoff energy is motivated from the formation enthalpy convergence calculations seen in Fig. S5 (ESI†). All structures were relaxed with respect to volume, shape, and internal atomic positions until an energy convergence of 10^{-6} eV per atom and a force convergence of 10^{-2} eV $Å^{-1}$ was reached. Density of states (DOS) and crystal orbital Hamilton population (COHP) were calculated using the LOBSTER[32–35] code where the calculated band-structure energy is reconstructed into orbital interactions. VESTA was used for visualizing the atomic structures.[36]

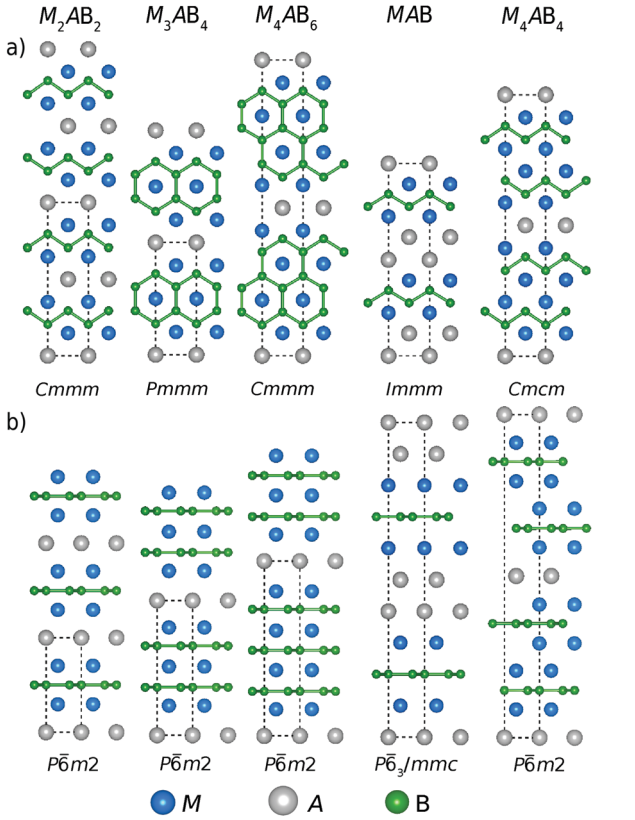

Fig. 1 Structural symmetries of the herein considered layered boride compositions, M_2AB_2, M_3AB_4, M_4AB_6, MAB and M_4AB_4, for structures with (a) orthorhombic and (b) hexagonal symmetry. The space group symmetry is denoted for each structure. Elements M, A, and B are represented by blue, grey, and green atoms.

The MAB compositions in focus are MAB, M_2AB_2, M_3AB_4, M_4AB_4 and M_4AB_6 in both orthorhombic and hexagonal space group symmetries, as shown in Fig. 1. The orthorhombic structures consist of the zigzag chains of boron while the hexagonal structures have boron in a flat honeycomb lattice. The hexagonal M_3AB_4, M_4AB_6, MAB and M_4AB_4 are hypothetical structures inspired symmetrically by the hexagonal Ti_2InB_2, where the considered composition and the stacking sequence is equivalent to their orthorhombic counterpart. The additional hypothetical hexagonal crystal structures of different stacking sequences were designed for the double layered MAB and M_4AB_4 compositions which can be observed in Fig. S6 (ESI†). The energy representing a specific phase is the crystal structure with the lowest energy. In this work we considered M from Groups 3 to 9; Sc, Y, Ti, Zr, Hf, V, Nb, Ta, Cr, Mo, W, Mn, Fe, and Co along with A elements; Al, Ga, and In, resulting in a total of 210 unique compositions and 420 MAB phases; *i.e.*, at each composition the MAB phase is represented by both orthorhombic

and hexagonal crystal structure symmetries. Additional information related to the considered crystal structures illustrated in Fig. 1 is found within Tables S2–S4 (ESI†).

Phase stability calculations

In this work, we express the stability of a MAB phases using two different variables evaluated at 0 K: formation energy[37–40] and formation enthalpy.[37–45] For a general $M_xA_yB_z$ phase, the formation energy, ΔE_f is calculated using

$$\Delta E_f\,(M_xA_yB_z) = E(M_xA_yB_z) - xE_M - yE_A - zE_B, \quad (1)$$

where $E(M_xA_yB_z)$ and E_i represents the calculated total energy of $M_xA_yB_z$ and single elements i = {M, A, B} in their ground-state crystal structure, respectively.

The second approach builds on comparing the energy of a general $M_xA_yB_z$ phase with respect to all possible linear combinations of competing phases present in the ternary M–A–B material system using an energy convex hull construction. At a given $M_xA_yB_z$ composition, the convex hull consists of competing phases that have an energy lower than any other combination of phases. Note that by definition, $M_xA_yB_z$ is not part of the convex hull construction. This set of competing phases represents the most favourable decomposition and is identified using a linear optimization procedure. This approach has previously been successful, both confirming experimental known materials as well as predicting new materials.[41–45] The set of most competing phases, commonly referred to as the equilibrium simplex, for a general $M_xA_yB_z$ composition, is obtained by solving

$$\min E_{cp}(b^M, b^A, b^B) = \sum_i^n x_i E_i \quad (2)$$

where b^M, b^A, b^B denotes the amount of each element M, A and B, and x_i and E_i denotes the amount and energy for a competing phase *i*. The minimized energy E_{cp}, representing the set of most competing phases, is then used to calculate the formation enthalpy, ΔH_{cp}, for $M_xA_yB_z$ using

$$\Delta H_{cp}(M_xA_yB_z) = E(M_xA_yB_z) - \min E_{cp}, \quad (3)$$

where $E(M_xA_yB_z)$ and E_{cp} is the calculated total energy of the $M_xA_yB_z$ phase and a linear combination of the identified equilibrium simplex, respectively. $M_xA_yB_z$ is considered stable if $\Delta H_{cp} < 0$ and not stable, or at best metastable, if $\Delta H_{cp} > 0$. Competing phases considered in this work were acquired from public databases such as OQMD,[46,47] Materials Project[48] and Springer Materials.[49]

Results and discussion

Theoretical phase stability of MAB phases

We start by evaluating different viewpoints for calculating stability at 0 K in Fig. 2 by comparing the formation energy, ΔE_f (eqn (1)), and the formation enthalpy, ΔH_{cp} (eqn (3)). The data represent the space group with the lowest energy for each $M_xA_yB_z$ composition. Experimentally synthesized phases are represented by black squares.

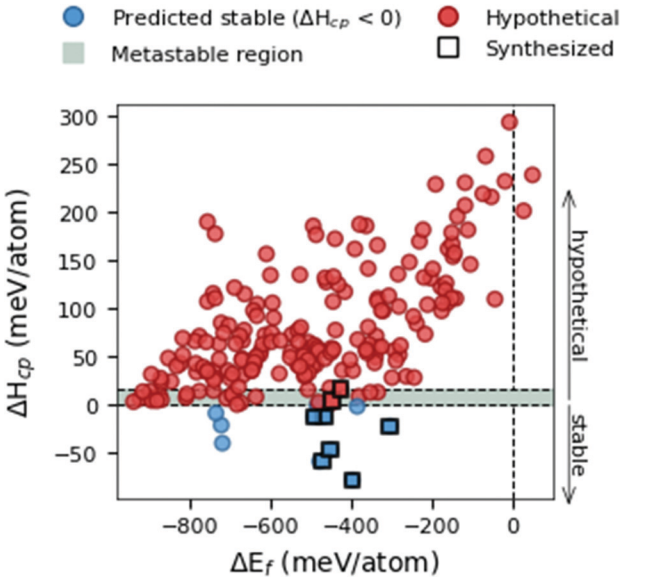

Fig. 2 Formation enthalpy, ΔH_{cp}, as a function of the formation energy, ΔE_f, for 210 MAB phase compositions. The data represent the space group with the lowest energy being either of hexagonal or orthorhombic symmetry. Synthesized phases are marked by a black square, hypothetical phases predicted stable ($\Delta H_{cp} < 0$) are marked by a blue circle, and hypothetical phases predicted not stable or at best metastable ($\Delta H_{cp} > 0$) are marked by a red circle. The metastable region $0 < \Delta H_{cp} < +17$ is denoted by the grey region.

Fig. 2 demonstrates the use of formation energy, ΔE_f, to be a rather poor indicator when predicting thermodynamical stability, compared to the formation enthalpy, ΔH_{cp}. Out of the 210 considered MAB phase compositions, all but two are found with $\Delta E_f < 0$. This indicates that 208 phases are stable with respect to decomposition into its constituent elements M, A and B. When formation enthalpy, ΔH_{cp}, is considered, only 10 phases are identified as thermodynamically stable with $\Delta H_{cp} < 0$. It is apparent that even though ΔE_f could indicate the stability of a phase it may be far from stable when compared to all competing phases in the material system. Out of the nine experimentally synthesized MAB phases, marked with black squares in Fig. 2, seven are found to be stable and two close to stable within $0 < \Delta H_{cp} < +17$. We use this information to define a metastable region, represented by a grey area in Fig. 1, where the upper limit is decided by the experimentally verified Cr_4AlB_6 with ΔH_{cp} = + 17 meV per atom. With this in mind, ΔH_{cp} is motivated as the better descriptor to be used for predicting the phase stability of hypothetical MAB phases yet to be synthesized.

Formation enthalpies of the M_2AB_2, M_3AB_4 and M_4AB_6 systems

The considered MAB phases in this work, illustrated in Fig. 1, can be divided into two subgroups based on their structural appearance; (i) M_2AB_2, M_3AB_4 and M_4AB_6 which only differ in the thickness of the M–B layer and can thus be described with the general $M_{n+1}AB_{2n}$ formula where n = 1, 2, 3 and (ii) MAB and M_4AB_4 with double layers of A and M, respectively.

We start by investigating the thermodynamic stability of the $M_{n+1}AB_{2n}$ phases with M = Sc, Y, Ti, Zr, Hf, V, Nb, Ta, Cr, Mo, W,

Mn, Fe, Co and A = Al, Ga, and In. Both orthorhombic and hexagonal structures are considered (see Fig. 1). Fig. 3 shows an overview of the calculated formation enthalpy ΔH_{cp} for $M_{n+1}AB_{2n}$, with the corresponding identified equilibrium simplex listed in Table S5 (ESI†). The thermodynamic stability is visualized using a heat map where the background colour represents ΔH_{cp} for the symmetry structure with the lowest energy where blue colour indicates a stable phase ($\Delta H_{cp} < 0$). A symbol representation is herein used to denote the structure of lowest energy; square for orthorhombic symmetry and hexagon for hexagonal symmetry. Experimentally synthesized phases are illustrated by a black square or a hexagon.

In Fig. 3a, we note that all experimentally known M_2AB_2 phases are found to be stable, *i.e.*, the orthorhombic M_2AlB_2 with M = Cr, Mn, Fe and hexagonal Ti_2InB_2. In addition, two hypothetical phases are predicted to be stable with a hexagonal structure symmetry, Zr_2InB_2 and Hf_2InB_2. These predictions are consistent with ref. 50. Hence, experimental verification is encouraged. Furthermore, four additional phases of the M_2AB_2 composition are predicted to be close to stable, $0 < \Delta H_{cp} < 17$ meV per atom, *i.e.*, Ti_2AlB_2, Ti_2GaB_2, Nb_2GaB_2 and Y_2InB_2.

For M_3AB_4 and M_4AB_6 compositions in Fig. 3b and c, only two phases are experimentally known, Cr_3AlB_4 and Cr_4AlB_6. These are found to be close to stable with ΔH_{cp} = 4 and 17 meV per atom, respectively. No phase is predicted stable, but 12 phases are found to be close to stable, $0 < \Delta H_{cp} < 17$ meV per atom, and includes the hypothetical phases with the hexagonal symmetries: Ti_4AlB_6, Ti_3GaB_4, Ti_4GaB_6, Ti_3InB_4, Ti_4InB_6, Zr_3InB_4, Zr_4InB_6, Hf_4AlB_6, Hf_4GaB_6, H_4InB_6, Nb_3GaB_4, Nb_4GaB_6. This is in contrast to a previous study where Ti_3AlB_4, Ti_3GaB_4 and Ti_3InB_4 were reported as thermodynamical stable. This discrepancy, between our results with those in ref. 10, can be associated with the limited consideration of competing phases being A = Al, Ga, In, TiB, and Ti_3B_4 in ref. 10 whereas in this work all known phases within each ternary system are considered. This example demonstrates the importance of an extensive analysis including all competing phases for conclusive theoretical predictions.

In Fig. 3, M from Groups 3 to 5 mainly results in hexagonal symmetry with the lowest energy and this is for all considered A-elements and $M_{n+1}AB_{2n}$ compositions. Similar observations can be made for group 6 metals with A = Ga and In. Out of the 126 compositions in Fig. 3, 97 are identified with hexagonal symmetry of lowest energy. Orthorhombic symmetries are mainly found for A = Al.

Formation enthalpy of MAB and M_4AB_4 systems

The following section focuses on the MAB phases with double layers of A and M, *i.e.*, the MAB and M_4AB_4 compositions. Again, both orthorhombic and hexagonal symmetries are considered (see Fig. 1). Fig. 4 shows an overview of the calculated formation enthalpy ΔH_{cp} for MAB and M_4AB_4, with the corresponding identified equilibrium simplex listed in Table S6 (ESI†). Again, the thermodynamic stability is visualized using a heat map with the background colour representing ΔH_{cp} for the symmetry with the lowest energy, where the blue colour indicates thermodynamical stability ($\Delta H_{cp} < 0$), and the structure of lowest energy is represented by a square for orthorhombic symmetry and a hexagon for hexagonal symmetry. Experimentally synthesized phases are marked by a black square.

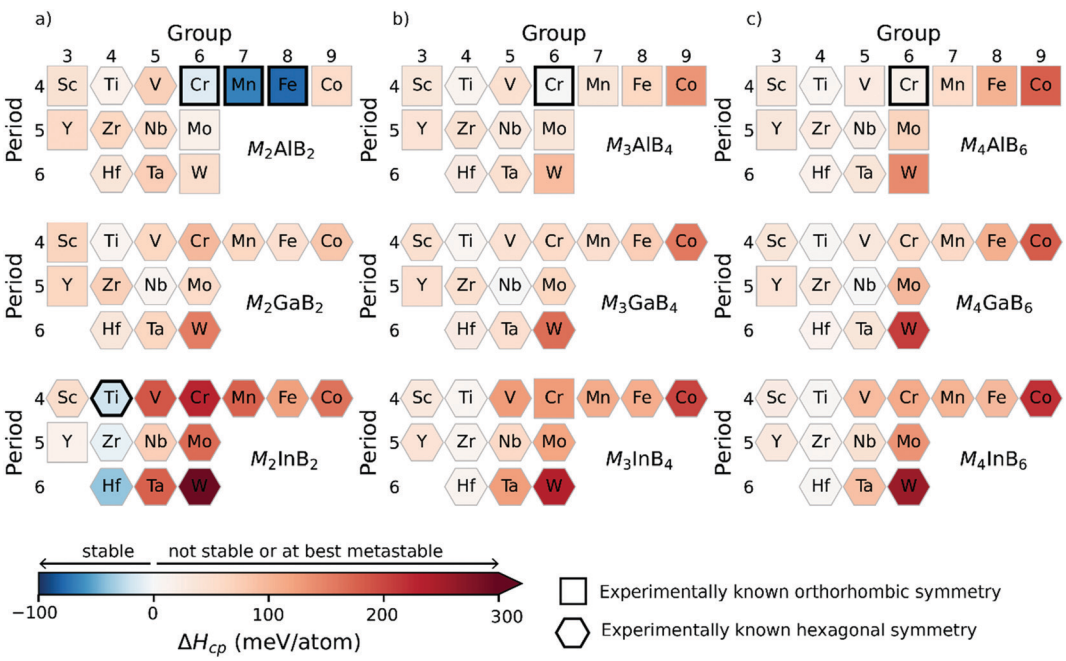

Fig. 3 Calculated formation enthalpies, ΔH_{cp}, for (a) M_2AB_2, (b) M_3AB_4, and (c) M_4AB_6 compositions showing whether the orthorhombic (square) or the hexagonal (hexagon) symmetry is the lowest in enthalpy. Experimentally known phases are marked with a black square or a hexagon.

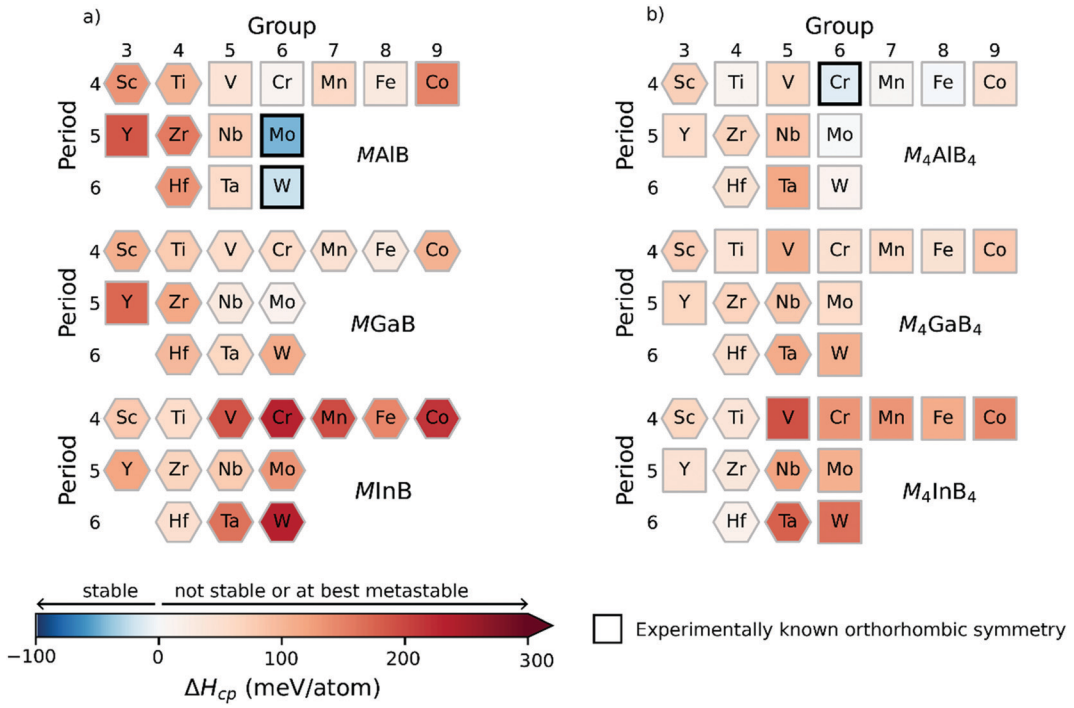

Fig. 4 Calculated formation enthalpies, ΔH_{cp}, for (a) MAB and (b) M_4AB_4 compositions showing whether orthorhombic (square) or hexagonal (hexagon) symmetry has the lowest energy. Experimentally known phases are marked with a black square.

In Fig. 4a, only two MAB phases are found to be stable, MoAlB and WAlB, both with orthorhombic symmetry, and formation enthalpies $\Delta H_{cp} = -47$ and $\Delta H_{cp} = -22$ meV per atom, respectively. Both MoAlB and WAlB have also been synthesized.[18] Two additional phases, CrAlB and MoGaB, are found to be close to stable with $\Delta H_{cp} = 9$ and 13 meV per atom, respectively. Similar to $M_{n+1}AB_{2n}$ in Fig. 3, the majority of MAB phases are identified with the hexagonal symmetry as the energetically preferred crystal structure of the considered M_4AB_4 phases in Fig. 4b, only two are predicted to be stable, the already synthesized Cr_4AlB_4 of orthorhombic symmetry ($\Delta H_{cp} = -12$ meV per atom)[19] and the hypothetical Mo_4AlB_4 ($\Delta H_{cp} = -1$ meV per atom). Five additional M_4AB_4 phases are identified to be close to stable, *i.e.*, Ti_4AlB_4, W_4AlB_4, Mn_4AlB_4, Fe_4AlB_4, and Hf_4InB_4.

A noteworthy observation in Fig. 4b is the energetically preferred crystal structure for M_4AB_4 phases is dominated by the orthorhombic symmetry, in contrast to $M_{n+1}AB_{2n}$ and MAB where the majority of phases are found with hexagonal symmetry. This is observed for all A-elements. Fig. 4 shows that 46 out of the 84 considered phases resulted in a crystal structure of hexagonal symmetry with the lowest energy.

The general observation from Fig. 3 and 4 is that hexagonal symmetries are typically preferred for M of Groups 3 to 5 and orthorhombic symmetries for A = Al. However, it should be noted that the displayed information only represents the crystal symmetry with the lowest energy. We therefore choose to further inspect the difference in energy between the hexagonal and orthorhombic symmetries as a step towards attaining an understanding of the preferred symmetry with various compositions and chemistries. Fig. 5 demonstrates the energy difference, ΔE(symmetry) = E(ort) − E(hex), where $\Delta E > 0$ indicates the hexagonal symmetry to be of lowest energy and is thus favoured whereas $\Delta E < 0$ indicates the orthorhombic symmetry to be favoured.

In Fig. 5 we find that most structures with A = Al yields an orthorhombic symmetry with the lowest energy. This contrasts with A = Ga and In where the hexagonal symmetry is the dominating symmetry with the lowest energy. For $M_{n+1}AB_{2n}$ phases (blue colours), the energetic preference for the hexagonal symmetry is found to generally increase in the series Al–Ga–In. Phases with M from Group 4 and 5 for A = Ga and In always have the hexagonal space group symmetry with the lowest energy. The exception among the compositions considered here is found for M_4AB_4, where the orthorhombic symmetry is most common and this is true for all considered A-elements. Note that M_4AB_4 have double-layered M (see Fig. 1) and thus their layer sequence differs from the other considered compositions.

From the results in Fig. 5 we find some trends both among the structural compositions like $M_{n+1}AB_{2n}$ and for different M and A. One hypothesis for this may be related to their underlying binary substructures. A short survey of experimentally binary metal borides reveal that hexagonal structures are more common at high boron content while orthorhombic structures are mainly observed at lower boron content. A summary of experimentally metal boride binary phases and their space group symmetries are listed in Table S7 (ESI†). This underlying feature may in part explain the observed trends in Fig. 5. To reveal other tendencies which may explain the trends in Fig. 5,

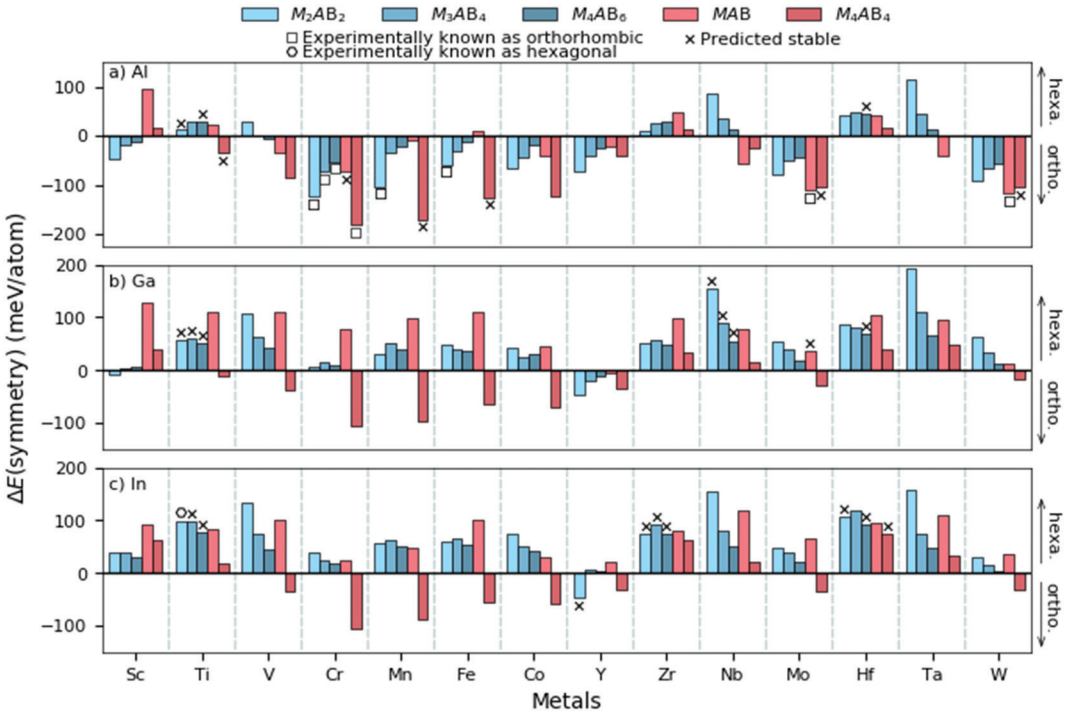

Fig. 5 The energy difference between the orthorhombic and hexagonal crystal symmetries, ΔE(symmetry), as a function of M for (a) A = Al, (b) A = Ga, and (c) A = In. $\Delta E > 0$ represent the hexagonal symmetry of lowest energy and $\Delta E < 0$ the orthorhombic symmetry of lowest energy. The colours represent different compositions where $M_{n+1}AB_{2n}$ compositions are in gradients of blue and double layered compositions in red. The experimentally known structures of orthorhombic symmetry are marked with a square and hexagonal symmetry with a hexagon. The theoretically predicted stable phases are marked with a cross.

we try to find any correlation between ΔE(symmetry) and the atomic size, electron concentration and electronegativity. However, no clear correlation is found, as shown in Fig. S6 (ESI†). In an initial attempt to explain the results of the symmetry preference in Fig. 5, we performed a bonding analysis for a selected set of M_2AB_2 phases with M = Sc, Ti, V, and Cr and A = Al and In, considering both hexagonal and orthorhombic symmetries using the Local Orbital Hamiltonian Suit Towards Electronic Structure Reconstruction (LOBSTER) code.[32–35] The total density of states (DOS) and its correlation with the total crystal orbital Hamiltonian population (COHP) for the considered M_2AB_2 phases is shown in Fig. S8 and S9 (ESI†). Furthermore, the total interaction within any of the considered orthorhombic symmetries is always greater than the hexagonal structure and this is independent of M or A, shown in Fig. S10 (ESI†). At this level, no distinct correlation between the populated anti-bonding and bonding states can be made in analogy with the symmetry preference in Fig. 5. A closer analysis of individual bonds, shown in Fig. S11 (ESI†), reveal stronger In–In bonds for the hexagonal structure as compared to the orthorhombic structure ($\sim$2.5 eV stronger). For phases with A = Al, the M–A bonds seem to play a more significant role, especially in Sc_2AlB_2 and Cr_2AlB_2, which both favours the orthorhombic symmetry. The brief bonding analysis of the selected phases considered herein indicates that the A-element interactions to play a crucial role in the symmetry preference.

Further attempts to enlighten the symmetry preference is made by comparing the calculated DOS and COHP of hexagonal and orthorhombic symmetries for the Ti_2InB_2 and Cr_2AlB_2 phases, shown in Fig. S12 and S13 (ESI†) along with a detailed analysis. For Ti_2InB_2 we find that the major difference between considered symmetries is the location of the Fermi level, which is close to a minimum for the hexagonal structure. For the orthorhombic structure there are many antibonding states just below the Fermi level which costs energy. This indicates overall why the hexagonal symmetry is lower in energy as compared to the orthorhombic structure. For Cr_2AlB_2, with the orthorhombic symmetry of lower energy than the hexagonal one, we find that the Cr 3d states around the Fermi level are non-bonding for the orthorhombic structure while being antibonding for the hexagonal structure. The latter have a destabilizing impact on its energy. This analysis gives a first glimpse of the electronic and bonding differences of M_2AB_2 and could, at least in part, explain the difference between hexagonal and orthorhombic symmetries.

Prediction using atomic size and electron concentration

The procedure for evaluating the thermodynamical stability of a given phase requires comparison of energies with a set of competing phases and can thus be quite demanding, especially when multiple compositions and elemental combinations are to be investigated. In order to determine the stability of a certain phase, its energy must be compared with the energy of all competing phases as done in Fig. 3 and 4. This procedure may be considered to be computationally demanding. Hence, alternative routes may be tempting to use for fast discovery of

new materials. One suggested approach is the so-called structure mapping methodology where the atomic size and electron concentration are used as descriptors for effortless predictions of a materials formability[20,21] or its properties.[22–24] Here we choose to test this hypothesis for predicting a material's possible existence or formability by using the same analysis as proposed in ref. 20 and 21. Adopted values of experimental atomic radii and number of valence/itinerant electrons for M, A, and B are retrieved from the ref. 51–53 and listed in Table S8 (ESI†).

The atomic size ratio of M- and A-element for $M_xA_yB_z$, as defined in ref. 20 is given by

$$\text{Atomic size ratio} = \frac{|R_M - R_A|}{R_M}, \quad (4)$$

where R_M and R_A is the atomic radius of elements M and A, respectively. Furthermore, the electron concentration (EC) for $M_xA_yB_z$, defined in ref. 20, is given by

$$\text{Electron concentration} = \frac{(\text{VEC})_M n_M + (e/a)_A n_A + (\text{VEC})_B n_B}{n_M + n_A + n_B}, \quad (5)$$

where $(\text{VEC})_i$ is the number of valence electrons of element i, where i = M, B, and $(e/a)_A$ is the itinerant electrons of the A-element. n_j symbolizes the elemental concentration for j = M, A, and B. Note that since the covalent M–B bonding is commonly stronger than the metallic M–A and B–A bonds, $(\text{VEC})_i$ is applied to the i = (M, B)-site elements while $(e/a)_A$ is used for the A-element. All approximations made are based on the approach suggested in ref. 20. In addition, we also include information from the stability predictions presented in Fig. 2–4 to find out if there is any correlation between these distinctly different approaches.

Fig. 6 shows the atomic size ratio as a function of electron concentration for all 210 compositions and where the difference between the two panels is how each data point is coloured. All experimentally synthesized phases are marked by black circles. In ref. 21, Shen *et al.* defined two lines to distinguish the most stable region, governed by $\frac{|R_m - R_A|}{R_A} < 0.4$ and an EC < 5.5, thus separating formable from non-formable phases which have been included within Fig. S7 (ESI†). Similarly, Zhang *et al.* introduced similar regions when investigating stability trends of MAX phases in ref. 20 As demonstrated in Fig. S14–S19 (ESI†) for each separate composition, using such lines is a rather crude approximation and do not give any valuable information.

In Fig. 6a, the data points are correlated with the calculated formation energy (eqn (1)) represented by a blue colour scale depending on its value. Note that 208 out of 210 phases are considered stable according to the ΔE_f approach. The large number of predicted stable phases in Fig. 6a in relation with the actual few experimentally synthesized phases indicate the ΔE_f approach to be a very crude approximation to the phase stability. One may speculate that the different compositions and structures considered herein and in ref. 21, may have an impact on the uncorrelated results. Corresponding figures for each considered composition are shown in Fig. S14–S19 (ESI†) where tendencies for a decrease in ΔE_f may correlate with a decrease of EC.

In Fig. 6b we include information from the calculated formation enthalpy (eqn (3)) to the atomic size ratio and the EC relationship. The corresponding colouring represents the value of ΔH_{cp} and range from blue (stable) to red (not stable).

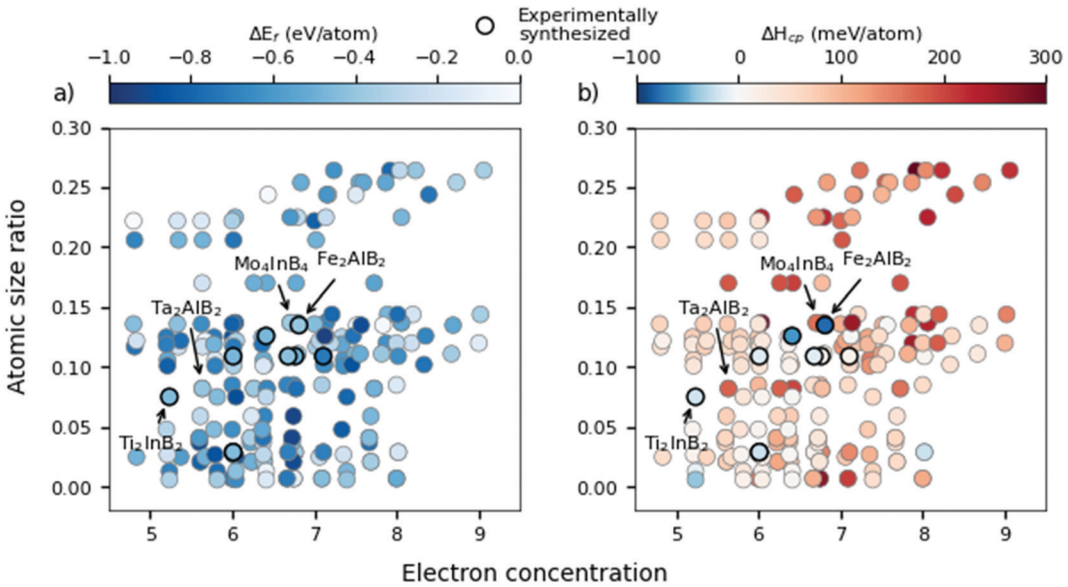

Fig. 6 The atomic size ratio as a function of the electron concentration where each data point represents the symmetry structure of lowest energy for all $M_xA_yB_z$ phases. Each data point in (a) and (b) is coloured based on their calculated ΔE_f and ΔH_{cp}, respectively. Experimentally synthesized phases are marked with a black circle. For comparison, four phases are explicitly marked: the synthesized and stable Fe_2AlB_2 and the hypothetical Mo_4InB_4 with similar size ratios and electron concentrations and the synthesized Ti_2InB_2 and far from stable Ta_2InB_2 of the same composition.

The situation in Fig. 6b is very different as compared to Fig. 6a. There is no correlation at all between the predicted stability and the atomic size, in additon to the EC, which verifies the uncertainty of using structure mapping methodology for materials predictions, at least for MAB phases. This becomes even more clear in Fig. S12 and S13 (ESI†) showing individual plots for each unique MAB composition. The only distinct result found is that a large enough atomic size ratio $\left(\frac{|R_m - R_A|}{R_A} > 0.15\right)$ combined with a high EC (EC $>$ 8) does result in phases far from being stable (ΔH_{cp} $>$ +140 meV per atom). Thus, the use of the structure mapping methodology for fast prediction of new materials gives misguiding information about possible phases suitable for future synthesis. This is explicitly demonstrated for two MAB phases of similar atomic size ratio and EC, Mo_4InB_4 and Fe_2AlB_2. Note that Fe_2AlB_2 is identified as stable (−78 meV per atom) indicated by the blue colour, and it has also been synthesized as indicated by the black circle. This is in contrast to the hypothetical Mo_4InB_4 which is far from being stable as indicated by the red colour (+107 meV per atom) yet has a similar size ratio and EC to Fe_2AlB_2. Additional contradictions between stable and unstable phases may be found within the M_2AB_2 system as demonstrated by comparing the experimentally verified Ti_2InB_2 (−21 meV per atom) and the far from stable Ta_2InB_2 (+177 meV per atom) both of which have similar size ratios and EC.

Based on the result shown in Fig. 6 and Fig. S12, S13 (ESI†), it is demonstrated here that even though it is tempting to use the structure mapping methodology for effortless predictions it does not reveal any valuable information about the possible existence or formability of MAB phases. It should be stressed that complete phase stability calculations, as shown in Fig. 3 and 4, are thus needed for reliable predictions of MAB phases, as demonstrated from verified stability for those already synthesized to date. Furthermore, the phase stability calculations also predict stable and close to stable phases not yet synthesized where experimental synthesis attempts are encouraged.

Conclusions

We have performed phase stability calculations on a total of 420 phases comprised of hexagonal and orthorhombic space group symmetries with MAB, M_2AB_2, M_3AB_4, M_4AB_4 and M_4AB_6 compositions where M = Sc, Y, Ti, Zr, Hf, V, Nb, Ta, Cr, Mo, W, Mn, Fe, and Co and A = Al, Ga, and In. The thermodynamical stability of the investigated compounds was evaluated in terms of both formation energy and formation enthalpy. The two alternative frameworks were compared and the formation enthalpy, ΔH_{cp}, is demonstrated as a superior alternative when evaluating the thermodynamical stability. 10 phases are predicted to be thermodynamically stable, out of which seven have previously been synthesized while Zr_2InB_2, Hf_2InB_2 and Mo_4AlB_4 are awaiting experimental verification. An additional 23 phases are close to stable ($0 < \Delta H_{cp} < 17$ meV per atom). By comparing the energy of orthorhombic and hexagonal structures we find that the majority of the $M_{1+n}AB_{2n}$ phases are found having the hexagonal symmetry of lowest energy when A = Ga and In while orthorhombic symmetry is of lowest energy when A = Al. Similar observations were made for the double layered MAB phases where the M_4AB_4 systems favour the orthorhombic symmetry. We have also critically examined the proposed structure mapping methodology for the fast prediction of new materials where the idea is to use the atomic size ratio and electron concentration as predictive descriptors. We conclude that it is an inappropriate approach which gives misguiding information about possible candidate phases for synthesis with no correlation at all to the calculated thermodynamical stability. This demonstrates the complexity of phase stability predictions and that shortcuts can give skewed results.

Conflicts of interest

There are no conflicts to declare.

Acknowledgements

M. D. acknowledges support from the Swedish Research council through project 2019-05047. J. R. acknowledges funding from the Knut and Alice Wallenberg (KAW) Foundation for a Fellowship/Scholar Grant and Project funding (KAW 2020.0033). The calculations were carried out using the supercomputer resources provided by the Swedish National Infrastructure for Computing (SNIC) at the National Supercomputer Center (NSC), the High Performance Computing Center North (HPC2N), and the PDC Center for High Performance Computing, partially founded by the Swedish Research Council through grant agreement no. 2018-05973.

References

1 J. Zhou, *et al.*, Boridene: two-dimensional $Mo_{4/3}B_{2-x}$ with ordered metal vacancies obtained by chemical exfoliation., *Science*, 2021, **373**(6556), 801–805.
2 S. Kota, M. Sokol and M. W. Barsoum, A progress report on the MAB phases: atomically laminated, ternary transition metal borides, *Int. Mater. Rev.*, 2020, **65**(4), 226–255.
3 A. Ahmed, *et al.*, Belt abrasion resistance and cutting tool studies on new ultra-hard boride materials, *Tribol. Int.*, 2009, **42**(5), 706–713.
4 C. Martini, *et al.*, Sliding and abrasive wear behaviour of boride coatings, *Wear*, 2004, **256**(6), 608–613.
5 I. E. Campos-Silva and G. A. Rodríguez-Castro, in *Boriding to improve the mechanical properties and corrosion resistance of steels, Thermochemical Surface Engineering of Steels*, ed. E. J. Mittemeijer and M. A. J. Somers, Woodhead Publishing, Oxford, 2015, pp. 651–702.
6 M. Khazaei, *et al.*, Novel MAB phases and insights into their exfoliation into 2D MBenes, *Nanoscale*, 2019, **11**(23), 11305–11314.
7 Z. Jiang, *et al.*, MBene (MnB): a new type of 2D metallic ferromagnet with high Curie temperature, *Nanoscale Horiz.*, 2018, **3**(3), 335–341.

8 X. Guo, *et al.*, Establishing a Theoretical Landscape for Identifying Basal Plane Active 2D Metal Borides (MBenes) toward Nitrogen Electroreduction, *Adv. Funct. Mater.*, 2021, **31**(6), 2008056.
9 L. T. Alameda, *et al.*, Topochemical Deintercalation of Al from MoAlB: Stepwise Etching Pathway, Layered Intergrowth Structures, and Two-Dimensional MBene, *J. Am. Chem. Soc.*, 2018, **140**(28), 8833–8840.
10 J. Wang, *et al.*, Discovery of hexagonal ternary phase Ti_2InB_2 and its evolution to layered boride TiB, *Nat. Commun.*, 2019, **10**(1), 2284.
11 H. Zhang, *et al.*, Phase pure and well crystalline Cr_2AlB_2: a key precursor for two-dimensional CrB, *J. Mater. Sci. Technol.*, 2019, **35**(8), 1593–1600.
12 M. W. Barsoum, The $M_{N+1}AX_N$ phases: A new class of solids: Thermodynamically stable nanolaminates, *Prog. Solid State Chem.*, 2000, **28**(1), 201–281.
13 A. Vahid Mohammadi, J. Rosen and Y. Gogotsi, The world of two-dimensional carbides and nitrides (MXenes), *Science*, 2021, **372**(6547), eabf1581.
14 M. Naguib, *et al.*, Two-Dimensional Nanocrystals Produced by Exfoliation of Ti_3AlC_2, *Adv. Mater.*, 2011, **23**(37), 4248–4253.
15 I. E. B. Aronsson, X-ray investigations on Me–Si–B systems (Me = Mn, Fe, Co). II. Some features of the Fe–Si–B and Mn–Si–B systems, *Acta Chem. Scand.*, 1960, **14**, 1403–1413.
16 H. Rohde and H. Kudielka, Strukturuntersuchungen an Carbosulfiden von Titan und Zirkon, *Z. Kristallogr. - Cryst. Mater.*, 1960, **114**(1–6), 447–456.
17 M. Sokol, *et al.*, On the Chemical Diversity of the MAX Phases, *Trends Chem.*, 2019, **1**(2), 210–223.
18 M. Ade and H. Hillebrecht, Ternary Borides Cr_2AlB_2, Cr_3AlB_4, and Cr_4AlB_6: The First Members of the Series $(CrB_2)_nCrAl$ with n = 1, 2, 3 and a Unifying Concept for Ternary Borides as MAB-Phases., *Inorg. Chem.*, 2015, **54**(13), 6122–6135.
19 H. Zhang, *et al.*, Crystal structure of Cr_4AlB_4: a new MAB phase compound discovered in Cr–Al–B system., *J. Mater. Sci. Technol.*, 2019, **35**(4), 530–534.
20 Y. Zhang, *et al.*, The role of Hume-Rothery's rules play in the MAX phases formability, *Materialia*, 2020, **12**, 100810.
21 C. Shen, *et al.* Designing of Magnetic MAB Phases for Energy Applications, 2020, arXiv:2009.14543.
22 X. Gu, *et al.*, Sorting transition-metal diborides: new descriptor for mechanical properties, *Acta Mater.*, 2021, **207**, 116685.
23 D. V. Rybkovskiy, *et al.*, Structure, Stability, and Mechanical Properties of Boron-Rich Mo–B Phases: A Computational Study, *J. Phys. Chem. Lett.*, 2020, **11**(7), 2393–2401.
24 K. Kádas, *et al.*, AlM_2B_2(M = Cr, Mn, Fe, Co, Ni): a group of nanolaminated materials, *J. Phys.: Condens. Matter*, 2017, **29**(15), 155402.
25 P. E. Blöchl, Projector augmented-wave method, *Phys. Rev. B: Condens. Matter Mater. Phys.*, 1994, **50**(24), 17953–17979.
26 G. Kresse and D. Joubert, From ultrasoft pseudopotentials to the projector augmented-wave method, *Phys. Rev. B: Condens. Matter Mater. Phys.*, 1999, **59**(3), 1758–1775.
27 G. Kresse and J. Hafner, Ab initio molecular dynamics for liquid metals, *Phys. Rev. B: Condens. Matter Mater. Phys.*, 1993, **47**(1), 558–561.
28 G. Kresse and J. Furthmüller, Efficient iterative schemes for ab initio total-energy calculations using a plane-wave basis set, *Phys. Rev. B: Condens. Matter Mater. Phys.*, 1996, **54**(16), 11169–11186.
29 J. P. Perdew, K. Burke and M. Ernzerhof, Generalized Gradient Approximation Made Simple, *Phys. Rev. Lett.*, 1996, **77**(18), 3865–3868.
30 A. Poulou, T. A. Mellan and M. W. Finnis, Stability of Zr–Al–C and Ti–Al–C MAX phases: a theoretical study, *Phys. Rev. Mater.*, 2021, **5**(3), 033608.
31 H. J. Monkhorst and J. D. Pack, Special points for Brillouin-zone integrations., *Phys. Rev. B: Condens. Matter Mater. Phys.*, 1976, **13**(12), 5188–5192.
32 R. Nelson, *et al.*, LOBSTER: Local orbital projections, atomic charges, and chemical-bonding analysis from projector-augmented-wave-based density-functional theory, *J. Comput. Chem.*, 2020, **41**(21), 1931–1940.
33 V. L. Deringer, A. L. Tchougreeff and R. Dronskowski, Crystal orbital Hamilton population (COHP) analysis as projected from plane-wave basis sets, *J. Phys. Chem. A*, 2011, **115**(21), 5461–5466.
34 R. Dronskowski and P. E. Bloechl, Crystal orbital Hamilton populations (COHP): energy-resolved visualization of chemical bonding in solids based on density-functional calculations, *J. Phys. Chem.*, 1993, **97**(33), 8617–8624.
35 S. Maintz, *et al.*, Analytic projection from plane-wave and PAW wavefunctions and application to chemical-bonding analysis in solids, *J. Comput. Chem.*, 2013, **34**(29), 2557–2567.
36 K. Momma and F. Izumi, VESTA 3 for three-dimensional visualization of crystal, volumetric and morphology data., *J. Appl. Crystallogr.*, 2011, **44**(6), 1272–1276.
37 M. Ashton, *et al.*, Computational discovery of stable M_2AX phases., *Phys. Rev. B*, 2016, **94**(5), 054116.
38 D. Horlait, *et al.*, Synthesis and DFT investigation of new bismuth-containing MAX phases, *Sci. Rep.*, 2016, **6**(1), 18829.
39 M. Khazaei, *et al.*, Electronic properties and applications of MXenes: a theoretical review, *J. Mater. Chem. C*, 2017, **5**(10), 2488–2503.
40 Z. M. Wong, *et al.*, Computational Discovery of Transparent Conducting In-Plane Ordered MXene (i-MXene) Alloys, *Chem. Mater.*, 2019, **31**(11), 4124–4132.
41 P. Eklund, *et al.*, Discovery of the Ternary Nanolaminated Compound Nb_2GeC by a Systematic Theoretical-Experimental Approach, *Phys. Rev. Lett.*, 2012, **109**(3), 035502.
42 M. Dahlqvist and J. Rosen, Predictive theoretical screening of phase stability for chemical order and disorder in quaternary 312 and 413 MAX phases, *Nanoscale*, 2020, **12**(2), 785–794.
43 F.-Z. Dai, *et al.*, $M_2M'AlB_4$ (M = Mn, Fe, Co, M′ = Cr, Mo, W): Theoretical predicted ordered MAB phases with Cr_3AlB_4 crystal structure, *J. Mater. Sci. Technol.*, 2019, **35**(7), 1432–1438.

44 M. Dahlqvist, *et al.*, Phase stability of Ti_2AlC upon oxygen incorporation: a first-principles investigation, *Phys. Rev. B: Condens. Matter Mater. Phys.*, 2010, **81**(2), 024111.
45 L. A. Hanner, *et al.*, Synthesis, characterization and first principle modelling of the MAB phase solid solutions: $(Mn_{1-x}Cr_x)_2AlB_2$ and $(Mn_{1-x}Cr_x)_3AlB_4$, *Mater. Res. Lett.*, 2021, **9**(2), 112–118.
46 S. Kirklin, J. E. Saal, B. Meredig, A. Thompson, J. W. Doak, M. Aykol, S. Rühl and C. Wolverton, The Open Quantum Materials Database (OQMD): assessing the accuracy of DFT formation energies, *npj Comput. Mater.*, 2015, **1**, 15010.
47 J. E. Saal, S. Kirklin, M. Aykol, B. Meredig and C. Wolverton, Materials Design and Discovery with High-Throughput Density Functional Theory: The Open Quantum Materials Database (OQMD), *JOM*, 2013, **65**, 1501–1509.
48 A. Jain, S. P. Ong, G. Hautier, W. Chen, W. D. Richards, S. Dacek, S. Cholia, D. Gunter, D. Skinner, G. Ceder and K. A. Persson, The Materials Project: a materials genome approach to accelerating materials innovation, *APL Mater.*, 2013, **1**, 011002.
49 Springer Materials: The Landolt-Börnstein database.
50 N. Miao, *et al.*, Computational Prediction of Boron-Based MAX Phases and MXene Derivatives, *Chem. Mater.*, 2020, **32**(16), 6947–6957.
51 W. A. Deskin, Inorganic chemistry: principles of structure and reactivity (Huheey, James E.), *J. Chem. Educ.*, 1973, **50**(7), A379.
52 N. N. Greenwood and A. Earnshaw, *Chemistry of the Elements*, 2nd edn, 1997.
53 U. Mizutani and H. Sato, Determination of electrons per atom ratio for transition metal compounds studied by FLAPW-Fourier calculations, *Philos. Mag.*, 2016, **96**(29), 3075–3096.

